

1 **The Role of Sediment-induced Light Attenuation on Primary Production during Hurricane Gustav**
2 **(2008)**

3
4 **Zhengchen Zang^{1, +}, Z. George Xue^{1,2,3 *}, Kehui Xu^{1,3}, Samuel J. Bentley^{3,4},**
5 **Qin Chen⁵, Eurico J. D'Sa^{1,3}, Le Zhang¹, Yanda Ou¹**

6
7 ¹ Department of Oceanography and Coastal Sciences, Louisiana State University, Baton Rouge,
8 LA 70803, USA

9 ⁺ current address: Department of Biology, Woods Hole Oceanographic Institution, Woods Hole,
10 MA, 02543

11 ² Center for Computation and Technology, Louisiana State University, Baton Rouge, LA 70803,
12 USA

13 ³ Coastal Studies Institute, Louisiana State University, Baton Rouge, LA 70803, USA

14 ⁴ Department of Geology and Geophysics, Louisiana State University, Baton Rouge, LA 70803,
15 USA

16 ⁵ Department of Civil and Environmental Engineering, Northeastern University, Boston, MA
17 02115, USA

18
19 Corresponding author: Z. George Xue (zxue@lsu.edu)

20
21 **Key Words:**

22 Gulf of Mexico; Sediment-induced light attenuation; hurricane; offshore bloom.

25 Abstract

26

27 We introduced a sediment-induced light attenuation algorithm into a biogeochemical model of the
28 Coupled Ocean-Atmosphere-Wave-Sediment Transport (COAWST) modeling system. A fully
29 coupled ocean-atmospheric-sediment-biogeochemical simulation was carried out to assess the
30 impact of sediment-induced light attenuation on primary production in the northern Gulf of Mexico
31 during the passage of Hurricane Gustav in 2008. When compared with model results without
32 sediment-induced light attenuation, our new model showed a better agreement with satellite data
33 on both the magnitude of nearshore chlorophyll concentration and the spatial distribution of
34 offshore bloom. When Gustav approached, resuspended sediment shifted the inner shelf ecosystem
35 from a nutrient-limited one to light-limited. One week after Gustav's landfall, accumulated
36 nutrient and favorable optical environment induced a post-hurricane algal bloom in the top 20 m
37 of water column, while the productivity in the lower water column was still light-limited due to
38 slow-settling sediment. Corresponding with the elevated offshore NO_3 flux (38.71 mmol N/m/s)
39 and decreased chlorophyll flux (43.10 mg/m/s), the outer shelf post-hurricane bloom should be
40 resulted from the cross-shelf nutrient supply instead of the lateral dispersed chlorophyll. Sensitivity
41 tests indicated that sediment light attenuation efficiency affected primary production when
42 sediment concentration was moderately high. Model uncertainties due to colored dissolved organic
43 matter and parameterization of sediment-induced light attenuation are also discussed.

44

45 1 Introduction

46 Light, nutrient and temperature play a vital role in photosynthesis and marine ecosystems.
47 The vertical structure of light availability in an aquatic environment is mainly modulated by the
48 shading effects of chlorophyll, colored dissolved organic matter (CDOM), detritus, and sediment
49 (Cloern, 1987; Devlin et al., 2008; Schaeffer et al., 2011; Ganju et al., 2014; McSweeney et al.,
50 2017). The optical environment in river-dominated shelves are more complex due to the interaction
51 between riverine inputs and regional hydrodynamics (Bierman et al., 1994; Lin et al., 2009; Zhu
52 et al., 2009). As the largest river in North America, the Mississippi-Atchafalaya River system
53 delivers 380 km^3 of freshwater and 115 Mt of sediments each year into the northern Gulf of Mexico
54 (nGoM; Meade and Moody, 2010; Allison et al., 2012). Along the Louisiana-Texas shelf in the
55 nGoM, suspended sediment concentration (SSC) in the water column exhibits strong seasonality:
56 high in winter and spring seasons due to strong sediment resuspension and high fluvial sediment
57 discharge, while largely reduced in summer and fall owing to the relatively low river inputs and
58 weak resuspension (Zang et al., 2019). Episodic hurricane events in summer and fall can disturb
59 vertical stratification and resuspend large amount of shelf sediment (D'Sa et al., 2011; Xu et al.,
60 2016; Zang et al., 2018). Enhanced resuspension during a hurricane might greatly change the shelf
61 ecosystem via modifying light availability. In addition, enhanced organic matter remineralization
62 in the bottom boundary layer could also introduce sharp changes to the ecosystem (Wilson et al.,
63 2013; Hurst et al., 2019). Yet studies of the impact from hurricane-induced resuspension are still
64 limited due to the challenge of *in-situ* data collection under extreme weather conditions.

65 As an alternative tool to fill the spatial and temporal gaps in *in-situ* datasets, coupled
66 physical-biogeochemical models have been widely applied to the Gulf of Mexico (GoM; e.g.,
67 Fennel et al., 2008; Laurent et al., 2012; Xue et al., 2013; Yu et al., 2015; Gomez et al., 2018). In
68 these models, photosynthetically available radiation was estimated using a similar method, namely,
69 light availability decreasing exponentially with water depth and the concentrations of light
70 absorbers (e.g., sediment and CDOM) in the overlying water column. Due to the lack of long-term

71 observations of CDOM, however, its impact on the optical environment was either not included
72 (e.g., Fennel et al., 2006; Gomez et al., 2018) or simply expressed as a function of salinity (Justić
73 and Wang 2014). Although most of these studies considered sediment-induced light attenuation
74 when estimating primary production, the related parameterization was uniform over the entire
75 research domain and did not vary with sediment dynamics (e.g., Zhou et al., 2017; Thewes et al.,
76 2020). Such an oversimplified treatment of sediment-induced light attenuation could substantially
77 impact a model's robustness in river-dominated shelves that encompass a wide range of SSC. In
78 the nGoM, Justić and Wang (2014) tentatively employed a new scheme by connecting sediment-
79 induced light attenuation with river discharge (salinity) and hydrodynamics (bottom shear stress).
80 However, the horizontal distribution of SSC in a realistic environment is not necessarily correlated
81 with that of the freshwater plume, and the contribution of resuspension to SSC at different depths
82 might be significantly different (Xu et al., 2011, 2016).

83 Gustav was the first major hurricane that made a landfall in Louisiana after Katrina (2005).
84 It passed through the center of GoM and landed near Cocodrie, Louisiana on September 1st, 2008
85 as a Category 2 hurricane (Forbes et al., 2010). Sediment resuspension and transport were strong
86 during the passage of Gustav, and thick post-hurricane deposition (up to 40 cm) was simulated on
87 the inner shelf (Zang et al., 2018) and in the bays (Liu et al., 2018). Korobkin et al. (2009) identified
88 a post-Gustav algal bloom around the Mississippi Delta on satellite images. High respiration and
89 stratification after the landfall of Gustav was reported to be connected with possible hypoxia
90 development on the shelf (McCarthy et al., 2013).

91 In this study, we introduce a new biogeochemical model with sediment-induced light
92 attenuation to the three-way coupled (atmospheric-wave-ocean-sediment transport) Gustav model
93 (Zang et al., 2018). While sediment dynamics can also impact nutrient dynamics via changing the
94 intensity of remineralization near the bottom (Moriarty et al., 2018), the scope of this study is to
95 investigate the influence of suspended sediment on the optical environment and thus primary
96 production. The impact from elevated remineralization of resuspended particular organic matter
97 during hurricane events is not considered as detailed processes because relevant parameterizations
98 are still largely unknown. The objectives of this paper are to: 1) evaluate the impact of sediment-
99 induced light attenuation on the spatiotemporal variation of nutrient-phytoplankton dynamics
100 during a hurricane event; 2) explore the driving mechanism of the post-hurricane bloom on the
101 shelf; and 3) investigate the response of primary production to sediment optical characteristics.

102 103 **2 Model Description**

104 2.1 Physical, sediment and biogeochemical models

105 Our model covered the entire GoM (Fig. 1a) and was built on the coupled ocean-
106 atmosphere-wave-and-sediment transport (COAWST) modeling system (Warner et al., 2008,
107 2010). COAWST is an open source model platform that consists of three numerical models: the
108 Weather Research and Forecasting model (WRF; Skamarock et al., 2005), the Regional Ocean
109 Modeling System (ROMS; Shchepetkin and McWilliams, 2005; Haidvogel et al., 2008), and the
110 Simulating Waves Nearshore model (SWAN; Booij et al., 1999). The Community Sediment
111 Transport Modeling System (CSTMS) is included in ROMS to simulate sediment transport,
112 stratigraphy, and geomorphology. Model Coupling Toolkit (MCT; Jacob et al., 2005) enables the
113 interaction among these three models. The details of model setup and validation of the three-way
114 coupled hydrodynamic-sediment transport model (WRF-ROMS-SWAN-CSTMS) were described
115 in Zang et al. (2018), where four types of sediment (two cohesive and two non-cohesive) were
116 defined with different grain diameters and settling velocities. There were 40 sediment layers on

117 the sea floor with a total thickness of 1 m to resolve sediment bed erosion and deposition. The
118 driving force of sediment resuspension was determined by bottom shear stress induced by wave
119 and current. Readers are referred to Zang et al. (2018) for detailed hydrodynamic and sediment
120 validation.

121 Given the importance of diatom in phytoplankton community in the nGoM (Zhao and
122 Quigg, 2014), it is necessary to have both nitrogen and silicon cycles in the model. The
123 biogeochemical model in this study was largely built on the North Pacific Ecosystem Model for
124 Understanding Regional Oceanography (NEMURO; Kishi et al., 2007), which incorporated both
125 nitrogen and silicon flows. There were 11 state variables included in the model: nitrate, ammonium,
126 two types of phytoplankton (small and large), three types of zooplankton (microzooplankton,
127 mesozooplankton and predatory zooplankton), particulate and dissolved nitrogen, particulate silica,
128 and silicic acid concentration. River nutrient discharge during the hurricane were retrieved
129 from United States Geological Survey (USGS) Water Data for the Nation website
130 (<http://nwis.waterdata.usgs.gov>; Station 07374000). The growth of phytoplankton was driven by
131 water temperature, light availability, and nutrient concentration. Instantaneous remineralization of
132 particulate organic nitrogen at the bottom was estimated following Fennel et al. (2006). Our model
133 did not include phosphate because its limitation on primary production in the nGoM was mainly
134 between May to July (Laurent et al., 2012; Laurent and Fennel, 2014). We incorporated two types
135 of chlorophyll corresponding to the large and small phytoplankton tracers, respectively. Following
136 Fennel et al. (2006), chlorophyll dynamics was derived from phytoplankton equation by
137 multiplying the ratio of chlorophyll to phytoplankton biomass. To get an ideal parameterization
138 set and a stable initial condition for the biogeochemical variables, we first conducted a 20-yr (1993-
139 2012) coupled physical-biogeochemical simulation using only ROMS model, where WRF and
140 SWAN were disabled to achieve a feasible computation load (Step 1 in Fig. 2). The atmospheric
141 forcing was provided by the 6-hourly, 38 km horizontal resolution Climate Forecast System
142 Reanalysis (CFSR; Saha et al., 2010, 2011; <http://cfs.ncep.noaa.gov>). The physical setup of the
143 20-yr simulation was the same as Zang et al. (2019). The biogeochemical parameterizations (Table
144 S1) were largely adapted after a recent GoM biogeochemical modeling study by Gomez et al.
145 (2018). Since this study focused on the response of biogeochemical process to hurricane events,
146 details of the 20-yr simulation setup and model-observation comparison, including time series of
147 water-level and chlorophyll, vertical profiles of nutrients, spatial distributions of chlorophyll,
148 diatom to total phytoplankton ratio, and mesozooplankton, were provided in the supplementary
149 material. Once validated, the biogeochemical variables were extracted from the 20-yr model on
150 August 30th, 2008 as the initial condition for this Gustav simulation (Step 2 in Fig. 2).

151 The light available for photosynthesis (I) is estimated using the following equation
152 (McSweeney et al., 2017):

$$153$$
$$154 \quad I = I_0 \cdot par \cdot \exp \left\{ -Z \left[\alpha_w + \alpha_{chl} \int_z^0 (PSn + PLn) dz + \alpha_{sed} \int_z^0 SSC dz \right] \right\},$$

155

156 where I_0 is the light intensity at the surface layer, and Z is water depth. par is the fraction of light
157 available for photosynthesis (specified as 0.43). α_w and α_{chl} are the light attenuation coefficients
158 of sea water and chlorophyll, respectively. PSn and PLn represent concentrations of small and
159 large phytoplankton. Compared with the original biogeochemical model, we added a new
160 sediment-induced light attenuation term in this equation. α_{sed} is the light attenuation coefficient
161 due to suspended sediment, and SSC is total suspended sediment concentration in the respective

162 layer. We performed a benchmark run ($\alpha_{sed} = 0.059$; McSweeney et al., 2017) to represent the
163 scenarios with sediment-induced light attenuation. The simulation period was from August 30th to
164 September 10th, 2008.

165 166 2.2 Sensitivity tests

167 High turbidity in the Mississippi River Delta due to fluvial sediment discharge and resuspension
168 suggested the vital role of sediment in the underwater optical environment. To quantitatively
169 evaluate the importance of suspended sediment in light attenuation, we conducted a sensitivity test
170 (test 1) without sediment-induced light attenuation ($\alpha_{sed} = 0$). Since the physical properties of a
171 sediment particle (e.g., size, shape, roughness, and color) determine its light attenuation efficiency
172 (Baker and Lavelle, 1984; Storlazzi et al., 2015), a wide range of α_{sed} (0.025–0.075) has been
173 reported in previous studies (e.g., Pennock, 1985; Van Duin et al., 2001; Arndt et al., 2007;
174 McSweeney et al., 2017). Here we increased/decreased the benchmark α_{sed} (0.059) by 20% and
175 40% to examine the sensitivity of primary production to sediment-induced light attenuation (tests
176 2–5). The rest of the model setup were the same between the benchmark run and sensitivity tests
177 (tests 1-5). The deviation due to the chaotic nature of turbulence was not considered in this study.
178

179 3 Model Validation

180 Direct measurements of ocean conditions during the passage of a hurricane are still
181 challenging. In Zang et al. (2018) we validated the physical model's performance against the air
182 pressure, sea level, and wave heights recorded at available buoy stations. The sediment model's
183 performance was evaluated against satellite images. In this study, we used the five-day composites
184 of SeaWiFS chlorophyll data (OC4) obtained before (Aug 25th–29th) and after (September 5th–9th)
185 Gustav's landing to calibrate our biogeochemical model's initial condition and results. Surface
186 chlorophyll distribution during initial condition (Fig. 3a) was similar to that in the pre-hurricane
187 composite imagery (Fig. 3b), with high chlorophyll concentration ($> 4 \text{ mg/m}^3$) located around the
188 bird-foot delta and the Atchafalaya inner shelf, and values declined seaward to $\sim 0.1 \text{ mg/m}^3$.

189 Compared with the pre-hurricane composite imagery, the post-hurricane composite
190 showed higher chlorophyll concentration around the bird-foot delta and on the Atchafalaya shelf
191 (Figs. 3b and 3c). Another major increase was identified in waters between the 50 and 200 m
192 isobaths off the Atchafalaya Bay with chlorophyll concentration increasing from 1 to 4 mg/m^3 after
193 Gustav, indicating a possible post-hurricane algal bloom on the outer shelf. When comparing with
194 model run without sediment-induced attenuation, the intensity of the offshore bloom was better
195 reproduced ($\sim 4 \text{ mg/m}^3$) with the new sediment-induced light attenuation algorithm (see difference
196 between Figs. 3d and 3e). To quantitatively evaluate the model's performance, we calculated the
197 root mean square error (RMSE) and correlation coefficient (R) between model-simulated and
198 satellite-derived chlorophyll concentrations over the inner shelf (water depth $< 50 \text{ m}$; Fig. 4). The
199 reduced RMSE in the benchmark run in comparison to sensitivity test (2.33 to 1.91) suggested
200 improved model performance with sediment-induced light attenuation. However, with only
201 marginal differences in the correlation coefficients between the two experiments (0.82 and 0.81),
202 the spatial distributions of chlorophyll were comparable (Fig. 4). Nevertheless, the model's
203 performance in the high productivity waters (both simulated and observed chlorophyll
204 concentrations $> 1 \text{ mg/m}^3$) was significantly improved (R increased from 0.55 to 0.61, and RMSE
205 decreased from 5.93 to 3.97; Fig. 4). The improvement of model results confirmed the importance
206 of sediment-induced light attenuation in biogeochemical cycling during a hurricane event,
207 particularly in coastal regions where chlorophyll concentration was high.

208

209 4 Results and Discussion

210 4.1 Temporal variability of biogeochemical variables

211 To examine the temporal variation of biogeochemical variables during the passage of
212 Gustav, we plotted the time series of spatially averaged net primary production (growth of
213 phytoplankton minus the respiratory losses; NPP), surface chlorophyll concentration, surface NO₃
214 concentration, SSC, downward solar short wave radiation, and sea surface temperature (SST) over
215 the nGoM inner shelf (Fig. 5; < 50 m water depth). NPP exhibited strong diel variation and the
216 peaks were strongly correlated with short wave radiation maximum (Figs. 5a and 5e). Such diel
217 cycle could also be found in chlorophyll concentration, but with a 3- to 4-hour delay (Fig. 5b).
218 Before the arrival of Gustav, daily-averaged NPP was around 0.05 g C/m²/hr, and the differences
219 of NPP and chlorophyll concentration between the benchmark run and test 1 were minor (Figs. 5a
220 and 5b).

221 Following hurricane Gustav's landfall along coastal Louisiana at 16:00:00 UTC on
222 September 1st, surface SSC increased to 3.8 kg/m³ because of strong seabed resuspension (Fig. 5d).
223 Daily-averaged NPP reduced to 0.03 g C/m²/hr in test 1. Once sediment-induced light attenuation
224 was included, daily-averaged NPP further declined to 0.01 g C/m²/hr, suggesting that light
225 availability severely limited short-term productivity on the inner shelf. Chlorophyll concentrations
226 in the benchmark run and test 1 were reduced by 40% as Gustav approached. Hurricane-related
227 surface cooling, together with decreased light (Figs. 5e and 5f), contributed to the reductions of
228 both chlorophyll and NPP.

229 The difference of daily-averaged NPP between the benchmark run and test 1 maximized
230 on September 2nd due to light limitation modulated by resuspended sediment (Figs. 5a and 5d). On
231 September 3rd, daily-averaged NPP of test 1 recovered to 0.04 g C/m²/hr and remained steady
232 through the end of our simulation (Fig. 5a). For the benchmark run, however, the recovery of NPP
233 was much slower: daily-averaged NPP was lower than that of test 1 until September 7th, when most
234 suspended sediment settled back onto the seabed. NO₃ concentration went up gradually between
235 September 2nd - 7th in the benchmark run (Fig. 5c) as nutrient consumption was constrained by the
236 decline in photosynthetic activity. Accumulated NO₃, together with the improved optical
237 environment due to low SSC, resulted in higher NPP and algal bloom after September 7th (Figs.
238 5a and 5b).

239

240 4.2 Vertical structure of biogeochemical variables

241 We extracted concentrations of chlorophyll, NO₃, sediment and water density anomaly
242 along the transect D in Rabalais et al. (2001; Fig. 1b for transect location) at three time points
243 (August 31st, September 2nd, and September 10th) to represent pre-, during-, and post-hurricane
244 stages, respectively (Figs. 6 and 7). Before the approach of Gustav, offshore water was well
245 stratified (Fig. 7d). Chlorophyll concentration decreased seaward from 5 to 0.3 mg/m³ (Figs. 6a
246 and 6d). Sediment-induced light attenuation did not alter the vertical structure of chlorophyll and
247 NO₃ much (Figs. 6a, 6d, 6g, and 6j) owing to low SSC in the water column (Fig. 7a). On September
248 2nd, strong vertical mixing increased the SSC to more than 1 kg/m³ over the entire water column
249 (Figs. 7b and 7e). Chlorophyll concentration in waters < 40 m in the benchmark run was ~ 4 mg/m³,
250 lower than that in test 1 due to sediment-induced light attenuation (Figs. 6b and 6e). Higher NO₃
251 concentration in the benchmark run was a result of the weakened primary production and nutrient
252 consumption (Figs. 6h and 6k). The most striking differences of chlorophyll and NO₃ between the
253 two simulations were in water shallower than 20 m.

254 In test 1, chlorophyll concentration during the post-hurricane stage was lower than that of
255 the pre-hurricane stage (Figs. 6a and 6c), in contrast to the condition captured by satellite imagery
256 (Figs. 3b and 3c). The benchmark run, however, successfully reproduced the magnitude and
257 seaward extension of the post-hurricane bloom (Fig. 6f). High chlorophyll concentration (> 1
258 mg/m^3 ; Fig. 6f) with low NO_3 (Fig. 6l) was simulated in the top 20 m of the water column where
259 stratification partially recovered (Fig. 7f) and sediment concentration was low after the passage of
260 Gustav (Fig. 7c). At water deeper than 20 m, chlorophyll concentration dropped drastically to less
261 than $0.1 \text{ mg}/\text{m}^3$, while NO_3 concentration further increased to $> 1 \text{ mmol}/\text{m}^3$. The synchronized
262 high turbidity and low chlorophyll concentration implied that, nine days after Gustav's landfall,
263 the primary production in deeper water could still be constrained by light availability. A similar
264 vertical structure (high SSC and low chlorophyll at the bottom) was also simulated in the Delaware
265 estuary, where near bottom productivity was constrained by the estuarine turbidity maximum
266 (McSweeney et al., 2017). Such a stratified water column with high/low productivity at the
267 surface/bottom is generally favorable for bottom oxygen depletion. The elevated surface
268 phytoplankton growth following the hurricane could thus result in increased particulate organic
269 matter (POM) whose remineralization contributes to bottom water hypoxia (Wiseman et al., 1997).
270 Meanwhile, the post-hurricane stratification recovery in the summer and fall seasons would have
271 likely prevented oxygen ventilation to the bottom. The high respiration rate caused by resuspended
272 POM could further lower the oxygen level (Bianucci et al., 2018). McCarthy et al. (2013) reported
273 a post-Gustav respiration peak associated with organic matter resuspension in the bottom boundary
274 layer. A recent numerical model study also simulated a substantial increase of near-bottom oxygen
275 consumption due to resuspended POM remineralization during moderate resuspension events
276 (Moriarty et al., 2018). These past studies and the new finding of this study suggest particulate
277 matter (both organic and inorganic) dynamics might substantially contribute to bottom oxygen
278 depletion and hypoxia development following a hurricane passage. More in situ observations of
279 oxygen dynamics in the bottom boundary layer are needed.

280

281 4.3 The post-hurricane offshore bloom

282 Post-hurricane blooms have been widely observed in the mid- and low-latitude oceans
283 (Davis and Yan, 2004; Miller et al., 2006; Pan et al., 2017; D'Sa et al. 2019). A bloom in the open
284 ocean was usually isolated and patchy, and its formation was mainly related to nutrients supplied
285 from deep waters via vertical mixing (Walker et al., 2005; Pan et al., 2017). The mechanism of the
286 bloom formation on the outer shelf, however, was more complex due to possible impacts from the
287 inner shelf water. Strong post-Gustav cross-shelf transport has been reported by previous studies
288 (Korobkin et al., 2009; Zang et al., 2018). The seaward dispersal of higher nutrient and chlorophyll
289 coastal waters could have potentially contributed to the outer shelf bloom, but their respective
290 contributions remained unclear. To quantify the cross-shore exported nutrient and chlorophyll, we
291 estimated depth-integrated offshore (seaward) NO_3 and chlorophyll flux along the 50 m isobath
292 transect (Fig. 1b; Table 1). Compared with test 1 (NO_3 : $7.35 \text{ mmol N}/\text{m}/\text{s}$; chlorophyll: 66.88
293 $\text{mg}/\text{m}/\text{s}$), the benchmark run estimated a higher NO_3 flux ($38.71 \text{ mmol N}/\text{m}/\text{s}$) and a lower
294 chlorophyll flux ($43.10 \text{ mg}/\text{m}/\text{s}$). The differences in NO_3 and chlorophyll fluxes between the two
295 simulations could be explained by nutrient accumulation and NPP reduction on the inner shelf
296 associated with resuspended sediment (Figs. 5a and 5c). Given the better offshore bloom intensity
297 reproduced by the benchmark run (Figs. 3d and 3e), we conclude the post-hurricane offshore
298 bloom was mainly triggered by nutrient exported from the inner shelf water.

299

300 4.4 Sensitivity to sediment light attenuation coefficient (α_{sed})

301 A wide range of particle physical properties (e.g., size, shape, roughness and color)
302 influence sediment light attenuation efficiency, which contributes to the difficulty in
303 parameterization of α_{sed} over a large region such as the nGoM (Baker and Lavelle, 1984; Storlazzi
304 et al., 2015). To examine the sensitivity of primary production to sediment light attenuation
305 efficiency, the results of sensitivity tests with different α_{sed} (tests 2–5) were compared against the
306 benchmark run.

307 Ahead of Gustav’s landfall, the difference in primary production between the benchmark
308 run and sensitivity tests was limited (Fig. 8a), which suggested that the nGoM ecosystem was
309 mainly limited by nutrient rather than light (Fennel et al., 2011). Two days after the landfall
310 (September 1st – 3rd), high SSC suppressed photosynthesis in the entire water column which
311 overwhelmed the response associated with different α_{sed} settings. As such, primary production
312 was not sensitive to α_{sed} from September 1st to 3rd, although the nGoM ecosystem was also light
313 limited. After September 3rd, the differences in primary production and NO₃ concentration
314 increased among the sensitivity tests through September 8th (Fig. 8). Primary production became
315 more sensitive to α_{sed} than SSC, which largely decreased due to settling (Fig. 5d). In the last two
316 days of our simulation, the primary production differences reduced again to pre-hurricane
317 conditions as the nGoM ecosystem shifted back to a nutrient-limited system.

318 In general, the influence of α_{sed} is significant when underwater light is limited by sediment
319 and SSC was moderately high. The optical environment over the muddy inner Louisiana shelf is
320 dominated by CDOM and chlorophyll under normal condition (D’Sa and Miller, 2003). During
321 energetic events (e.g., hurricanes, cold fronts), however, high concentrations of resuspended
322 sediment become the most important light absorber. Given the high frequency of cold fronts in
323 winter (once every 3–7 days) and energetic hurricanes in summer (Walker and Hammack, 2000;
324 Keim et al., 2007), it is reasonable to speculate that the ecosystem along coastal Louisiana would
325 be sensitive to α_{sed} not only on event scale, but also on seasonal to annual scales. The role of
326 long-term sediment dynamics in water clarity and marine ecology has been reported in other
327 regions (Dupont and Aksnes, 2013; Capuzzo et al., 2015; Wilson and Heath, 2019). To prove this
328 hypothesis in the nGoM, we need a long-term biogeochemical simulation that explicitly include
329 sediment-induced light attenuation effects in the future.

330

331 4.5 Model uncertainties

332 The optical environment over the muddy Louisiana shelf is dominated by phytoplankton,
333 suspended sediment, CDOM, and detritus particle (Le et al., 2014). The model presented in this
334 study only includes the light attenuation due to the former two constituents, and the potential
335 influence from CDOM and detritus warrants future study. Light attenuation due to CDOM was
336 simply parameterized using salinity in a previous model study (Justić and Wang, 2014), yet few
337 biogeochemical models incorporate dissolved/detritus-induced light attenuation. In the nGoM,
338 CDOM plays an indispensable role in modulating optical properties of inner shelf waters (D’Sa
339 and Miller, 2003; D’Sa et al. 2018), thus including CDOM-induced light attenuation would likely
340 lower the threshold of sediment resuspension above which the nGoM ecosystem would be light-
341 limited. To estimate the importance of CDOM-induced light attenuation in the biogeochemical
342 models, a long-term CDOM climatology is desired in the future.

343 We use SeaWiFS-derived chlorophyll concentration to evaluate model performance.
344 However, deriving high quality chlorophyll data during hurricanes is still a challenge because: 1)
345 the presence of thick clouds limits the availability and quality of satellite images (Huang et al.,

2011); 2) the uncertainty of chlorophyll estimation can be amplified by strong CDOM absorption (D'Sa and Miller, 2003; D'Sa et al., 2006); and 3) conducting chlorophyll measurements during a hurricane to calibrate bio-optical algorithms is limited by cost and safety. Given the rapid change and a wide range of sediment and chlorophyll concentrations after hurricanes, the algorithms based on observations under normal conditions might incur a bias. To achieve a high-quality satellite-derived chlorophyll data, it is essential to optimize an algorithm based on field observations during hurricane events.

In this study we simplified α_{sed} as a constant over the entire GoM. When water is highly turbid, the availability of light for photosynthesis could be more related to sediment concentration rather than α_{sed} (McSweeney et al., 2017). Thus, using a constant to represent the sediment light attenuation coefficient when sediment concentration is high should not introduce considerable bias. The optical characteristics of sediment particles, however, could greatly modify light availability underwater when SSC is relatively low (Storlazzi et al., 2015). Our sensitivity tests also suggest the importance of α_{sed} in photosynthesis and primary production as resuspended sediment settle back to the sea floor. Therefore, it is necessary to develop a spatially explicit α_{sed} to better parameterize the sediment's impact on light attenuation in future work.

Organic matter remineralization in sediment can dramatically increase nutrient concentration in the bottom boundary layer during strong resuspension (Couceiro et al., 2013). Field measurements after hurricanes Gustav and Ike suggested that the resuspension can expose the organic material in sediment to a more favorable environment for respiration (McCarthy et al., 2013). Nevertheless, so far most biogeochemical models either neglect or simply parameterize this process (Fennel et al., 2006; Chai et al., 2007; Kishi et al., 2007). Moriarty et al. (2018) developed a particulate organic matter resuspension model and found remineralization intensity increased by an order of magnitude during moderate resuspension events in the nGoM. Given the strong storm-driven resuspension during hurricanes, nutrient dynamics can be modified greatly by remineralization after the storm passage as well. Thus, incorporating organic matter resuspension and remineralization, in conjunction with the light attenuation effects addressed in this study, will help to improve our understanding of hurricane's impact on the biogeochemical cycling in shelf waters.

Our biogeochemical model include freshwater and terrestrial nutrient input via river channel. Du et al. (2019) estimated freshwater budget during hurricane Harvey and found that surface runoff and groundwater accounted for ~34% of the total freshwater load during the hurricane. Although our understanding of nutrient flux associated with these two types of freshwater inputs is still limited, excluding surface runoff and groundwater flux in the model implies our underestimation of terrestrial nutrient discharge from the land. Coupling groundwater and hydrology models with ocean model is a feasible way to achieve a comprehensive assessment of a hurricane's impact on the coastal and shelf ecosystem. In addition, water heating due to light absorption can also impact the ecosystem (Cahill et al., 2008; Mobley et al., 2015), but it has yet to be considered in our model.

385

386 **5 Conclusions**

387 We introduced a sediment-induced light attenuation algorithm to ROMS' biogeochemical
388 model. The new model reproduced the biogeochemical cycling during hurricane Gustav in the
389 northern Gulf of Mexico. Improved model performance suggested suspended sediment can play
390 an important role in underwater optical environment and primary production. During the passage
391 of Gustav, the high SSC changed the inner shelf from a nutrient-limited environment to a light-

392 limited one. NPP reduced from 0.05 to 0.01 g C/m²/hr, then recovered to pre-hurricane condition
393 after one week of hurricane landfall. As sediment further settled back on the seabed, nutrient
394 accumulation and increased light availability incurred a strong surface post-hurricane bloom on
395 the inner shelf. Nine days after Gustav's arrival, NPP below 20 m water depth was still light-
396 limited due to slow settling of sediment. The post-hurricane bloom on the outer shelf was
397 significantly enhanced by the laterally transported nutrient from inner to outer shelf. Suspended
398 sediment affected primary production when SSC was moderately high after Gustav's landfall. For
399 aquatic environments with great spatiotemporal variation of SSC (e.g., estuaries and lagoons), an
400 optimal parameterization of sediment-induced light attenuation is imperative to better evaluate
401 hurricane's impact on coastal productivity and biogeochemical cycling.

402

403 **Acknowledgements**

404 This study was supported by NSF CyberSEES Award CCF-1856359, NASA (award number
405 NNH17ZHA002C), Louisiana Board of Regents (award number NASA/LEQSF(2018-20)-
406 Phase3-11), NSF Coastal SEES Award 1427389, and the LSU Foundation Billy and Ann Harrison
407 Endowment for Sedimentary Geology. Computational support was provided by the High
408 Performance Computing Facility (cluster Supermike II) at Louisiana State University. Model
409 results used in this study are available at LSU mass storage system and details are on the webpage
410 of the Coupled Ocean Modeling Group at LSU (<http://www.oceanography.lsu.edu/xuelab>). Data
411 requests can be sent to the corresponding author via this webpage.

412

413 **References**

414

- 415 Allison, M.A., Demas, C.R., Ebersole, B.A., Kleiss, B.A., Little, C.D., Meselhe, E.A., Powell,
416 N.J., Pratt, T.C., Vosburg, B.M., 2012. A water and sediment budget for the lower
417 Mississippi-Atchafalaya River in flood years 2008-2010: Implications for sediment
418 discharge to the oceans and coastal restoration in Louisiana. *J. Hydrol.* 432–433, 84–97.
419 <https://doi.org/10.1016/j.jhydrol.2012.02.020>
- 420 Arndt, S., Vanderborght, J., Regnier, P., 2007. Diatom growth response to physical forcing in a
421 macrotidal estuary: Coupling hydrodynamics, sediment transport, and biogeochemistry. *J.*
422 *Geophys. Res. Ocean.* 112.
- 423 Baker, E.T., Lavelle, J.W., 1984. Effect of Particle Size on the Light Attenuation Coefficient of
424 Natural Suspensions. *J. Geophys. Res.* 89, 8197–8203.
425 <https://doi.org/10.1029/JC089iC05p08197>
- 426 Bianucci, L., Balaguru, K., Smith, R.W., Leung, L.R., Moriarty, J.M., 2018. Contribution of
427 hurricane-induced sediment resuspension to coastal oxygen dynamics. *Sci. Rep.* 8.
428 <https://doi.org/10.1038/s41598-018-33640-3>
- 429 Bierman, V.J., Hinz, S.C., Zhu, D., Wiseman, W.J., Rabalais, N.N., Turner, R.E., 1994. A
430 preliminary mass balance model of primary productivity and dissolved oxygen in the
431 Mississippi River plume/inner Gulf Shelf region. *Estuaries* 17, 886–899.
- 432 Booij, N., Ris, R.C., Holthuijsen, L.H., 1999. A third-generation wave model for coastal regions:
433 1. Model description and validation. *J. Geophys. Res. Ocean.* 104, 7649–7666.
- 434 Cahill, B., Schofield, O., Chant, R., Wilkin, J., Hunter, E., Glenn, S., Bissett, P., 2008. Dynamics
435 of turbid buoyant plumes and the feedbacks on near-shore biogeochemistry and physics.
436 *Geophys. Res. Lett.* 35, 1–6. <https://doi.org/10.1029/2008GL033595>
- 437 Capuzzo, E., Stephens, D., Silva, T., Barry, J., Forster, R.M., 2015. Decrease in water clarity of

438 the southern and central North Sea during the 20th century. *Glob. Chang. Biol.* 21, 2206–
439 2214. <https://doi.org/10.1111/gcb.12854>

440 Chai, F., Jiang, M.S., Chao, Y., Dugdale, R.C., Chavez, F., Barber, R.T., 2007. Modeling
441 responses of diatom productivity and biogenic silica export to iron enrichment in the
442 equatorial Pacific Ocean. *Global Biogeochem. Cycles* 21, 1–16.
443 <https://doi.org/10.1029/2006GB002804>

444 Cloern, J.E., 1987. Turbidity as a control on phytoplankton biomass and productivity in
445 estuaries. *Cont. Shelf Res.* 7, 1367–1381.

446 Couceiro, F., Fones, G.R., Thompson, C.E.L., Statham, P.J., Sivyer, D.B., Parker, R., Kelly-
447 Gerreyn, B.A., Amos, C.L., 2013. Impact of resuspension of cohesive sediments at the
448 Oyster Grounds (North Sea) on nutrient exchange across the sediment-water interface.
449 *Biogeochemistry* 113, 37–52. <https://doi.org/10.1007/s10533-012-9710-7>

450 D'Sa, E.J., Korobkin, M., Ko, D.S., 2011. Effects of Hurricane Ike on the Louisiana-Texas coast
451 from satellite and model data. *Remote Sens. Lett.* 2, 11–19.
452 <https://doi.org/10.1080/01431161.2010.489057>

453 D'Sa, E.J., Miller, R.L., 2003. Bio-optical properties in waters influenced by the Mississippi
454 River during low flow conditions. *Remote Sens. Environ.* 84, 538–549.
455 [https://doi.org/10.1016/S0034-4257\(02\)00163-3](https://doi.org/10.1016/S0034-4257(02)00163-3)

456 D'Sa, E.J., Miller, R.L., Del Castillo, C., 2006. Bio-optical properties and ocean color algorithms
457 for coastal waters influenced by the Mississippi River during a cold front. *Appl. Opt.* 45,
458 7410–7428.

459 D'Sa, E.J., Joshi, I.D., Liu, B., 2018. Galveston Bay and coastal ocean optical-geochemical
460 response to Hurricane Harvey from VIIRS ocean color. *Geophys. Res. Lett.* 45,
461 <https://doi.org/10.1029/2018GL079954>

462 D'Sa, E.J., Joshi, I.D., Liu, B., Ko, D.S., Osburn, C.L., Bianchi, T.S., 2019. Biogeochemical
463 response of Apalachicola Bay and the shelf waters to Hurricane Michael using ocean color
464 semi-analytic/inversion and hydrodynamic models. *Front. Mar. Sci.* 6:523,
465 [doi:10.3389/fmars.2019.00523](https://doi.org/10.3389/fmars.2019.00523)

466 Davis, A., Yan, X.H., 2004. Hurricane forcing on chlorophyll-a concentration off the northeast
467 coast of the U.S. *Geophys. Res. Lett.* 31, 4–7. <https://doi.org/10.1029/2004GL020668>

468 Devlin, M.J., Barry, J., Mills, D.K., Gowen, R.J., Foden, J., Sivyer, D., Tett, P., 2008.
469 Relationships between suspended particulate material, light attenuation and Secchi depth in
470 UK marine waters. *Estuar. Coast. Shelf Sci.* 79, 429–439.
471 <https://doi.org/10.1016/j.ecss.2008.04.024>

472 Du, J., Park, K., Dellapenna, T.M., Clay, J.M., 2019. Dramatic hydrodynamic and sedimentary
473 responses in Galveston Bay and adjacent inner shelf to Hurricane Harvey. *Sci. Total*
474 *Environ.* 653, 554–564. <https://doi.org/10.1016/j.scitotenv.2018.10.403>

475 Dupont, N., Aksnes, D.L., 2013. Centennial changes in water clarity of the baltic sea and the
476 north sea. *Estuar. Coast. Shelf Sci.* 131, 282–289. <https://doi.org/10.1016/j.ecss.2013.08.010>

477 Fennel, K., Hetland, R., Feng, Y., Dimarco, S., 2011. A coupled physical-biological model of the
478 Northern Gulf of Mexico shelf: Model description, validation and analysis of phytoplankton
479 variability. *Biogeosciences* 8, 1881–1899. <https://doi.org/10.5194/bg-8-1881-2011>

480 Fennel, K., Wilkin, J., Levin, J., Moisan, J., O'Reilly, J., Haidvogel, D., 2006. Nitrogen cycling
481 in the Middle Atlantic Bight: Results from a three-dimensional model and implications for
482 the North Atlantic nitrogen budget. *Global Biogeochem. Cycles* 20, 1–14.
483 <https://doi.org/10.1029/2005GB002456>

484 Fennel, K., Wilkin, J., Previdi, M., Najjar, R., 2008. Denitrification effects on air-sea CO₂ flux
485 in the coastal ocean: Simulations for the northwest North Atlantic. *Geophys. Res. Lett.* 35,
486 1–5. <https://doi.org/10.1029/2008GL036147>

487 Forbes, C., Luettich, R. a., Mattocks, C. a., Westerink, J.J., 2010. A Retrospective Evaluation of
488 the Storm Surge Produced by Hurricane Gustav (2008): Forecast and Hindcast Results.
489 *Weather Forecast.* 25, 1577–1602. <https://doi.org/10.1175/2010WAF2222416.1>

490 Ganju, N.K., Miselis, J.L., Aretxabaleta, A.L., 2014. Physical and biogeochemical controls on
491 light attenuation in a eutrophic, back-barrier estuary. *Biogeosciences* 11, 7193–7205.
492 <https://doi.org/10.5194/bg-11-7193-2014>

493 Gomez, F.A., Lee, S.K., Liu, Y., Hernandez, F.J., Muller-Karger, F.E., Lamkin, J.T., 2018.
494 Seasonal patterns in phytoplankton biomass across the northern and deep Gulf of Mexico: A
495 numerical model study. *Biogeosciences* 15, 3561–3576. <https://doi.org/10.5194/bg-15-3561-2018>

497 Haidvogel, D.B., Arango, H., Budgell, W.P., Cornuelle, B.D., Curchitser, E., Di Lorenzo, E.,
498 Fennel, K., Geyer, W.R., Hermann, A.J., Lanerolle, L., Levin, J., McWilliams, J.C., Miller,
499 A.J., Moore, A.M., Powell, T.M., Shchepetkin, A.F., Sherwood, C.R., Signell, R.P.,
500 Warner, J.C., Wilkin, J., 2008. Ocean forecasting in terrain-following coordinates:
501 Formulation and skill assessment of the Regional Ocean Modeling System. *J. Comput.*
502 *Phys.* 227, 3595–3624. <https://doi.org/10.1016/j.jcp.2007.06.016>

503 Huang, W., Mukherjee, D., Chen, S., 2011. Assessment of Hurricane Ivan impact on
504 chlorophyll-a in Pensacola Bay by MODIS 250m remote sensing. *Mar. Pollut. Bull.* 62,
505 490–498. <https://doi.org/10.1016/j.marpolbul.2010.12.010>

506 Hurst, N.R., White, J.R., Xu, K., Ren, M., 2019. Nitrate reduction rates in sediments
507 experiencing turbulent flow conditions. *Ecol. Eng.* 128, 33–38.
508 <https://doi.org/10.1016/j.ecoleng.2018.12.027>

509 Jacob, R., Larson, J., Everest, O., 2005. M x N Communication and Parallel Interpolation in
510 Community Climate System Model Version 3 Using the Model Coupling Toolkit. *Int. J.*
511 *High Perform. Comput. Appl.* 19, 293–307. <https://doi.org/10.1177/1094342005056116>

512 Justić, D., Wang, L., 2014. Assessing temporal and spatial variability of hypoxia over the inner
513 Louisiana-upper Texas shelf: Application of an unstructured-grid three-dimensional coupled
514 hydrodynamic-water quality model. *Cont. Shelf Res.* 72, 163–179.
515 <https://doi.org/10.1016/j.csr.2013.08.006>

516 Keim, B.D., Muller, R.A., Stone, G.W., 2007. Spatiotemporal patterns and return periods of
517 tropical storm and hurricane strikes from Texas to Maine. *J. Clim.* 20, 3498–3509.
518 <https://doi.org/10.1175/JCLI4187.1>

519 Kishi, M.J., Kashiwai, M., Ware, D.M., Megrey, B.A., Eslinger, D.L., Werner, F.E., Noguchi-
520 Aita, M., Azumaya, T., Fujii, M., Hashimoto, S., 2007. NEMURO—a lower trophic level
521 model for the North Pacific marine ecosystem. *Ecol. Modell.* 202, 12–25.

522 Korobkin, M., D’Sa, E., Ko, D.S., 2009. Satellite observations and NCOM assessment of the
523 Mississippi-Louisiana-Texas coast following hurricanes Gustav and Ike. *Ocean.* 2009 1–4.
524 <https://doi.org/10.23919/OCEANS.2009.5422213>

525 Laurent, A., Fennel, K., 2014. Simulated reduction of hypoxia in the northern Gulf of Mexico
526 due to phosphorus limitation. *Elementa* 2, 1–12.
527 <https://doi.org/10.12952/journal.elementa.000022>

528 Laurent, A., Fennel, K., Hu, J., Hetland, R., 2012. Simulating the effects of phosphorus
529 limitation in the Mississippi and Atchafalaya river plumes. *Biogeosciences* 9, 4707–4723.

530 <https://doi.org/10.5194/bg-9-4707-2012>

531 Le, C., Lehrter, J.C., Hu, C., Murrell, M.C., Qi, L., 2014. Spatiotemporal chlorophyll-a dynamics
532 on the Louisiana continental shelf derived from a dual satellite imagery algorithm. *J.*
533 *Geophys. Res. Ocean.* 119, 7449–7462.

534 Lin, S., Zou, T., Gao, H., Guo, X., 2009. The vertical attenuation of irradiance as a function of
535 turbidity: a case of the Huanghai (Yellow) Sea in spring. *Acta Oceanol. Sin.* 28, 66–75.

536 Liu, K., Chen, Q., Hu, K., Xu, K., Twilley, R.R., 2018. Modeling hurricane-induced wetland-bay
537 and bay-shelf sediment fluxes. *Coast. Eng.* 135, 77–90.
538 <https://doi.org/10.1016/j.coastaleng.2017.12.014>

539 McCarthy, M.J., Carini, S.A., Liu, Z., Ostrom, N.E., Gardner, W.S., 2013. Oxygen consumption
540 in the water column and sediments of the northern Gulf of Mexico hypoxic zone. *Estuar.*
541 *Coast. Shelf Sci.* 123, 46–53. <https://doi.org/10.1016/j.ecss.2013.02.019>

542 McSweeney, J.M., Chant, R.J., Wilkin, J.L., Sommerfield, C.K., 2017. Suspended-Sediment
543 Impacts on Light-Limited Productivity in the Delaware Estuary. *Estuaries and Coasts* 40,
544 977–993. <https://doi.org/10.1007/s12237-016-0200-3>

545 Meade, R.H., Moody, J.A., 2010. Causes for the decline of suspended-sediment discharge in the
546 Mississippi River system, 1940-2007. *Hydrol. Process.* 24, 35–49.

547 Miller, W.D., Harding, L.W., Adolf, J.E., 2006. Hurricane Isabel generated an unusual fall
548 bloom in Chesapeake Bay. *Geophys. Res. Lett.* 33, 2–5.
549 <https://doi.org/10.1029/2005GL025658>

550 Mobley, C.D., Chai, F., Xiu, P., Sundman, L.K., 2015. Impact of improved light calculations on
551 predicted phytoplankton growth and heating in an idealized upwelling-downwelling channel
552 geometry. *J. Geophys. Res. Ocean.* 120, 875–892.

553 Moriarty, J.M., Harris, C.K., Fennel, K., Friedrichs, M.A.M., Xu, K., Rabouille, C., 2017. The
554 roles of resuspension, diffusion and biogeochemical processes on oxygen dynamics
555 offshore of the Rhône River, France: A numerical modeling study. *Biogeosciences* 14,
556 1919–1946. <https://doi.org/10.5194/bg-14-1919-2017>

557 Moriarty, J.M., Harris, C.K., Friedrichs, M.A.M., Fennel, K., Xu, K., 2018. Impact of seabed
558 resuspension on oxygen and nitrogen dynamics in the northern Gulf of Mexico: A
559 numerical modeling study. *J. Geophys. Res. Ocean.* 1–27.
560 <https://doi.org/10.1029/2018JC013950>

561 Pan, G., Chai, F., Tang, D.L., Wang, D., 2017. Marine phytoplankton biomass responses to
562 typhoon events in the South China Sea based on physical-biogeochemical model. *Ecol.*
563 *Modell.* 356, 38–47. <https://doi.org/10.1016/j.ecolmodel.2017.04.013>

564 Pennock, J.R., 1985. Chlorophyll distributions in the Delaware estuary: regulation by light-
565 limitation. *Estuar. Coast. Shelf Sci.* 21, 711–725.

566 Rabalais, N.N., Turner, R.E., Wiseman, W.J., 2001. Hypoxia in the Gulf of Mexico. *J. Environ.*
567 *Qual.* 30, 320–329.

568 Saha, S., Moorthi, S., Pan, H.L., Wu, X., Wang, J., Nadiga, S., Tripp, P., Kistler, R., Woollen, J.,
569 Behringer, D., 2010. NCEP climate forecast system reanalysis (CFSR) 6-hourly products,
570 January 1979 to December 2010. *Res. Data Arch. Natl. Cent. Atmos. Res. Comput. Inf.*
571 *Syst. Lab. Boulder, CO.*

572 Saha, S., Moorthi, S., Wu, X., Wang, J., Nadiga, S., Tripp, P., Behringer, D., Hou, Y.T., Chuang,
573 H., Iredell, M., 2011. NCEP climate forecast system version 2 (CFSv2) 6-hourly products.
574 *Res. Data Arch. Natl. Cent. Atmos. Res. Comput. Inf. Syst. Lab.*

575 Schaeffer, B.A., Sinclair, G.A., Lehrter, J.C., Murrell, M.C., Kurtz, J.C., Gould, R.W., Yates,

576 D.F., 2011. An analysis of diffuse light attenuation in the northern Gulf of Mexico hypoxic
577 zone using the SeaWiFS satellite data record. *Remote Sens. Environ.* 115, 3748–3757.
578 <https://doi.org/10.1016/j.rse.2011.09.013>

579 Shchepetkin, A.F., McWilliams, J.C., 2005. The regional oceanic modeling system (ROMS): A
580 split-explicit, free-surface, topography-following-coordinate oceanic model. *Ocean Model.*
581 9, 347–404. <https://doi.org/10.1016/j.ocemod.2004.08.002>

582 Skamarock, W.C., Klemp, J.B., Dudhi, J., Gill, D.O., Barker, D.M., Duda, M.G., Huang, X.-Y.,
583 Wang, W., Powers, J.G., 2005. A Description of the Advanced Research WRF Version 3.
584 Tech. Rep. 113. <https://doi.org/10.5065/D6DZ069T>

585 Storlazzi, C.D., Norris, B.K., Rosenberger, K.J., 2015. The influence of grain size, grain color,
586 and suspended-sediment concentration on light attenuation: Why fine-grained terrestrial
587 sediment is bad for coral reef ecosystems. *Coral Reefs* 34, 967–975.
588 <https://doi.org/10.1007/s00338-015-1268-0>

589 Thewes, D., Stanev, E. V., Zielinski, O., 2020. Sensitivity of a 3D Shelf Sea Ecosystem Model to
590 Parameterizations of the Underwater Light Field. *Front. Mar. Sci.* 6.
591 <https://doi.org/10.3389/fmars.2019.00816>

592 Tweel, A.W., Turner, R.E., 2012. Landscape-Scale Analysis of Wetland Sediment Deposition
593 from Four Tropical Cyclone Events. *PLoS One* 7.
594 <https://doi.org/10.1371/journal.pone.0050528>

595 Van Duin, E.H.S., Blom, G., Los, F.J., Maffione, R., Zimmerman, R., Cerco, C.F., Dortch, M.,
596 Best, E.P.H., 2001. Modeling underwater light climate in relation to sedimentation,
597 resuspension, water quality and autotrophic growth. *Hydrobiologia* 444, 25–42.
598 <https://doi.org/10.1023/A:1017512614680>

599 Walker, N.D., Hammack, A.B., 2000. Impacts of winter storms on circulation and sediment
600 transport: Atchafalaya-Vermilion Bay region, Louisiana, USA. *J. Coast. Res.* 16, 996–1010.
601 <https://doi.org/10.2307/4300118>

602 Walker, N.D., Leben, R.R., Balasubramanian, S., 2005. Hurricane-forced upwelling and
603 chlorophyll a enhancement within cold-core cyclones in the Gulf of Mexico. *Geophys. Res.*
604 *Lett.* 32, 1–5. <https://doi.org/10.1029/2005GL023716>

605 Warner, J.C., Armstrong, B., He, R., Zambon, J.B., 2010. Development of a Coupled Ocean-
606 Atmosphere-Wave-Sediment Transport (COAWST) Modeling System. *Ocean Model.* 35,
607 230–244. <https://doi.org/10.1016/j.ocemod.2010.07.010>

608 Warner, J.C., Sherwood, C.R., Signell, R.P., Harris, C.K., Arango, H.G., 2008. Development of a
609 three-dimensional, regional, coupled wave, current, and sediment-transport model. *Comput.*
610 *Geosci.* 34, 1284–1306. <https://doi.org/10.1016/j.cageo.2008.02.012>

611 Wilson, R.F., Fennel, K., Paul Mattern, J., 2013. Simulating sediment-water exchange of
612 nutrients and oxygen: A comparative assessment of models against mesocosm observations.
613 *Cont. Shelf Res.* 63, 69–84. <https://doi.org/10.1016/j.csr.2013.05.003>

614 Wilson, R.J., Heath, M.R., 2019. Increasing turbidity in the North Sea during the 20th century
615 due to changing wave climate. *Ocean Sci.* 15, 1615–1625. [https://doi.org/10.5194/os-15-](https://doi.org/10.5194/os-15-1615-2019)
616 [1615-2019](https://doi.org/10.5194/os-15-1615-2019)

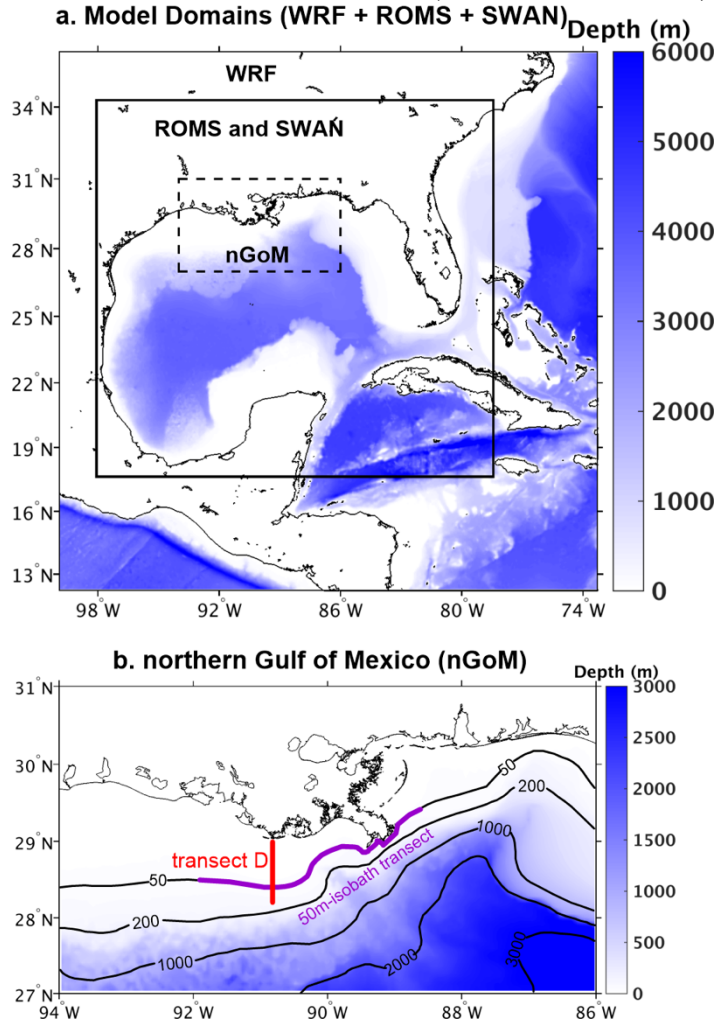
617 Wiseman, W.J., Rabalais, N.N., Turner, R.E., Dinnel, S.P., MacNaughton, A., 1997. Seasonal
618 and interannual variability within the Louisiana coastal current: stratification and hypoxia.
619 *J. Mar. Syst.* 12, 237–248.

620 Xu, K., Harris, C.K., Hetland, R.D., Kaihatu, J.M., 2011. Dispersal of Mississippi and
621 Atchafalaya sediment on the Texas-Louisiana shelf: Model estimates for the year 1993.

622 Cont. Shelf Res. 31, 1558–1575. <https://doi.org/10.1016/j.csr.2011.05.008>
623 Xu, K., Mickey, R.C., Chen, Q., Harris, C.K., Hetland, R.D., Hu, K., Wang, J., 2016. Shelf
624 sediment transport during hurricanes Katrina and Rita. *Comput. Geosci.* 90, 24–39.
625 <https://doi.org/10.1016/j.cageo.2015.10.009>
626 Xue, Z., He, R., Fennel, K., Cai, W.J., Lohrenz, S., Hopkinson, C., 2013. Modeling ocean
627 circulation and biogeochemical variability in the Gulf of Mexico. *Biogeosciences* 10, 7219–
628 7234. <https://doi.org/10.5194/bg-10-7219-2013>
629 Yu, L., Fennel, K., Laurent, A., 2015. A modeling study of physical controls on hypoxia
630 generation in the northern Gulf of Mexico. *J. Geophys. Res. Ocean.* 1–16.
631 <https://doi.org/10.1002/2014JC010472>. Received
632 Zang, Z., Xue, Z.G., Bao, S., Chen, Q., Walker, N.D., Haag, A.S., Ge, Q., Yao, Z., 2018.
633 Numerical study of sediment dynamics during hurricane Gustav. *Ocean Model.* 126, 29–42.
634 <https://doi.org/10.1016/j.ocemod.2018.04.002>
635 Zang, Z., Xue, Z.G., Xu, K., Bentley, S.J., Chen, Q., D'Sa, E.J., Ge, Q., 2019. A Two Decadal
636 (1993–2012) Numerical Assessment of Sediment Dynamics in the Northern Gulf of
637 Mexico. *Water* 11, 938.
638 Zhao, Y., Quigg, A., 2014. Nutrient limitation in Northern Gulf of Mexico (NGOM):
639 Phytoplankton communities and photosynthesis respond to nutrient pulse. *PLoS One* 9.
640 <https://doi.org/10.1371/journal.pone.0088732>
641 Zhou, F., Chai, F., Huang, D., Xue, H., Chen, J., Xiu, P., Xuan, J., Li, J., Zeng, D., Ni, X., Wang,
642 K., 2017. Investigation of hypoxia off the Changjiang Estuary using a coupled model of
643 ROMS-CoSiNE. *Prog. Oceanogr.* 159, 237–254.
644 <https://doi.org/10.1016/j.pocean.2017.10.008>
645 Zhu, Z., Ng, W., Liu, S., Zhang, J., Chen, J., Wu, Y., 2009. Estuarine phytoplankton dynamics
646 and shift of limiting factors: A study in the Changjiang (Yangtze River) Estuary and
647 adjacent area. *Estuar. Coast. Shelf Sci.* 84, 393–401.
648

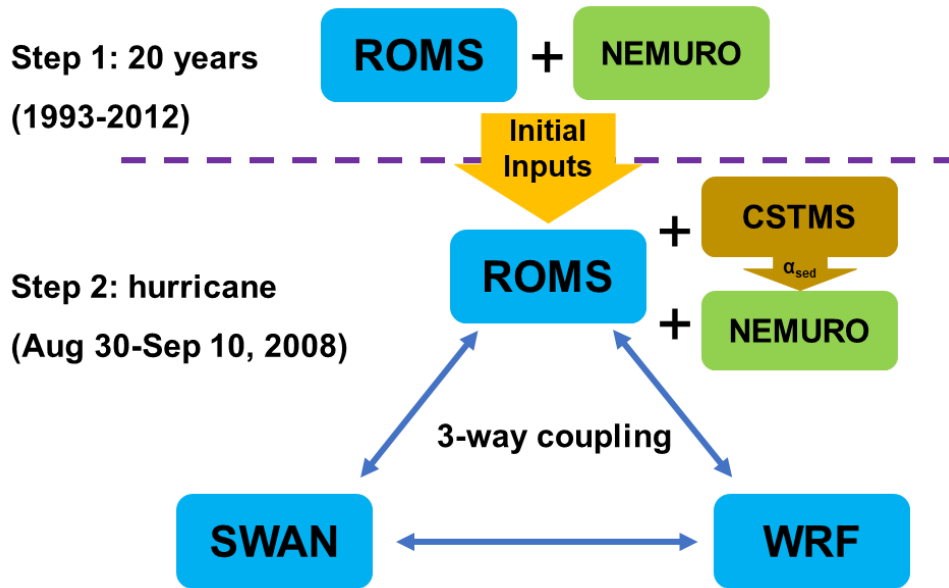
649
650
651
652
653
654

Figure 1. panel a: Model domains applied in this study. The entire panel a is the WRF model domain (6 km resolution) overlaid with water depth (color-shading). The black solid box represents the model grid used by ROMS and SWAN with 5 km resolution. The black dashed line box (lat: 27°N–31°N; lon: 94°W–86°W) covers the northern Gulf of Mexico (nGoM). More details in the nGoM are shown in panel b. The thick purple/red lines indicate locations of 50m-isobath transect and transect D (Rabalais et al., 2001), respectively.



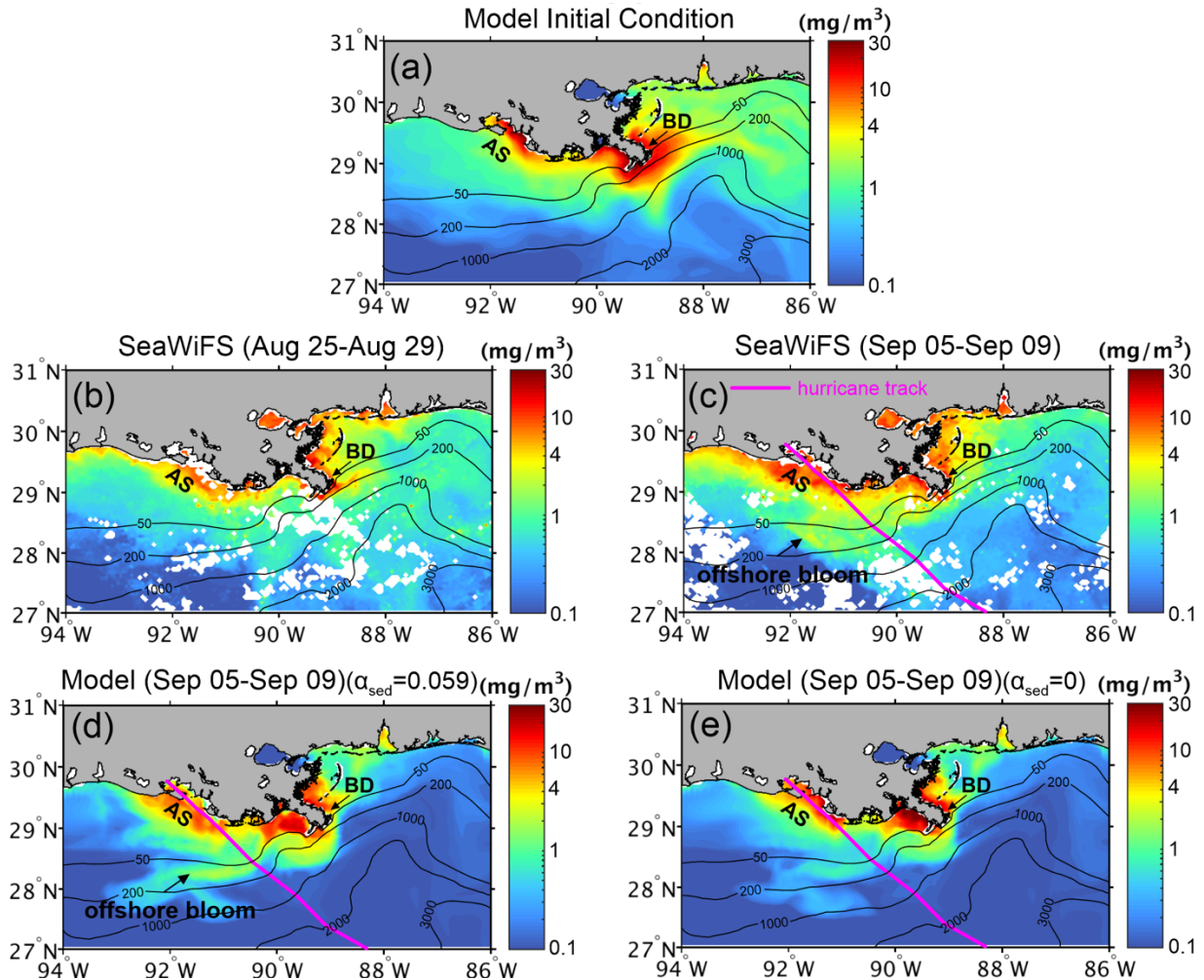
655
656

657 **Figure 2.** Flow chart of long-term (20 years) and hurricane (11 days) simulations. In Step 1 we
 658 only run ocean (ROMS) and biogeochemical (NEMURO) models, which provide initial inputs for
 659 the next step. Step 2 couples ocean (ROMS), wave (SWAN), atmosphere (WRF), sediment
 660 (CSTMS) and new biogeochemical (NEMURO) models with new sediment-induced light
 661 attenuation term.



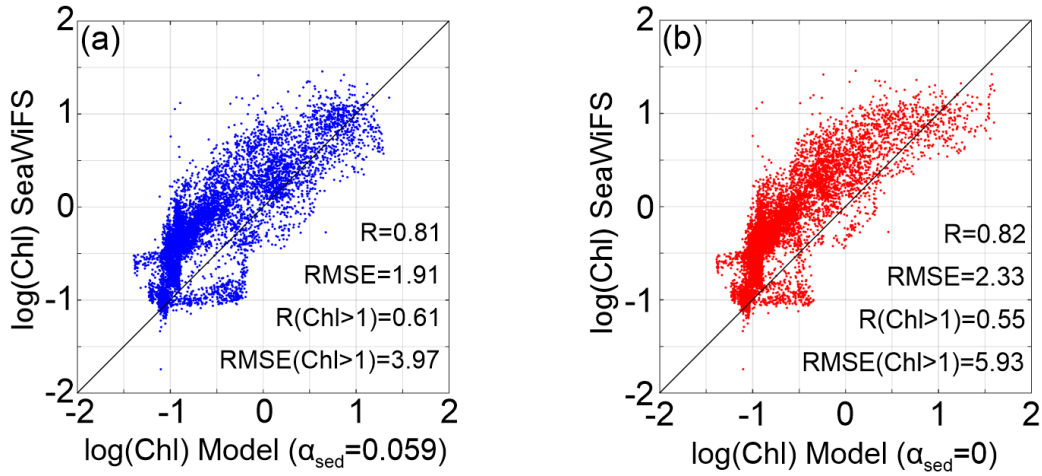
662
 663

664 **Figure 3.** Initial condition of surface chlorophyll extracted from 20-year simulation (a) and five-
 665 day composite of surface chlorophyll concentration in the year 2008: (b) SeaWiFS data before
 666 Gustav (August 25th–29th); (c) SeaWiFS data after Gustav (September 05th–09th); (d) benchmark
 667 run result ($\alpha_{sed} = 0.059$) after Gustav; (e) test 1 result ($\alpha_{sed} = 0$) after Gustav. White color in
 668 panels (b) and (c) represents no data. Magenta curve shows hurricane track in panels b, c, and d.
 669 (BD: bird-foot Mississippi delta; AS: Atchafalaya shelf).
 670



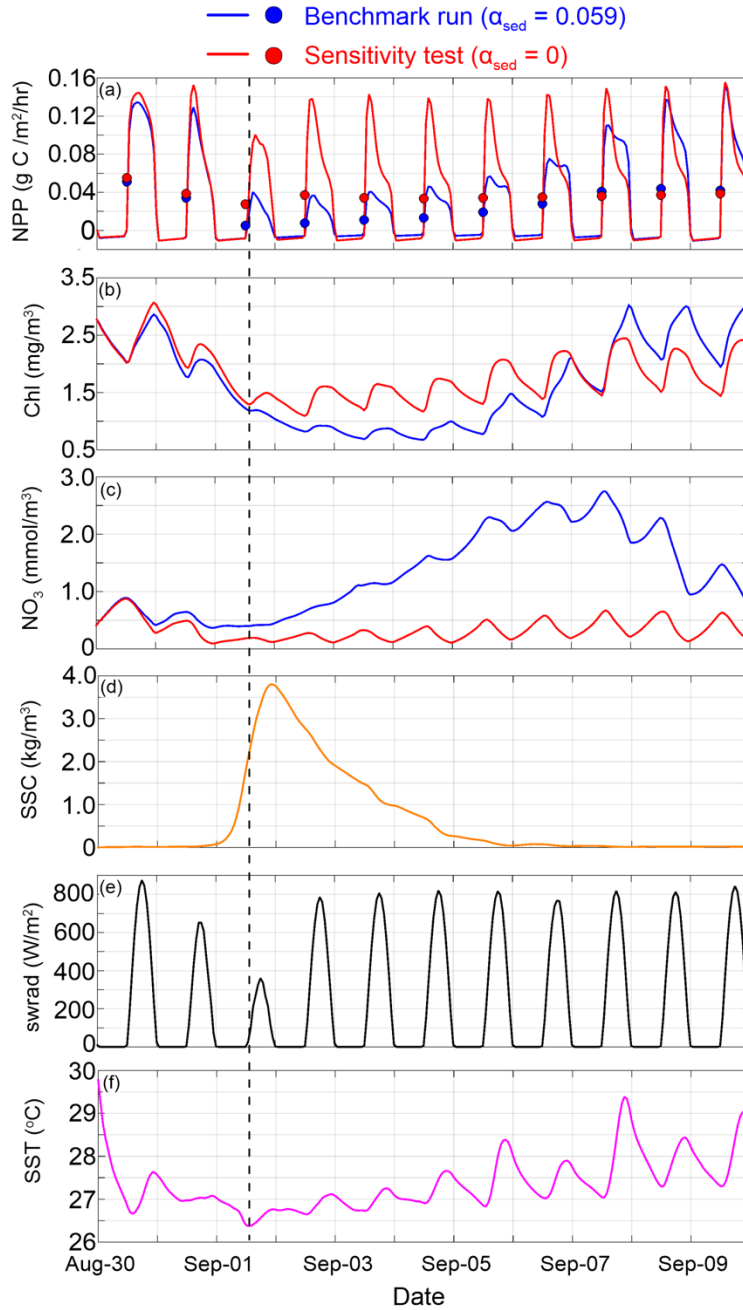
671
 672

673 **Figure 4.** Simulated five-day composite (September 05th–09th) of surface chlorophyll
674 concentration after hurricane Gustav compared to corresponding SeaWiFS-derived surface
675 chlorophyll results over the nGOM inner shelf ($h < 50$ m) for model results based on (a)
676 benchmark ($\alpha_{sed} = 0.059$) and (b) test 1 ($\alpha_{sed} = 0$) runs.



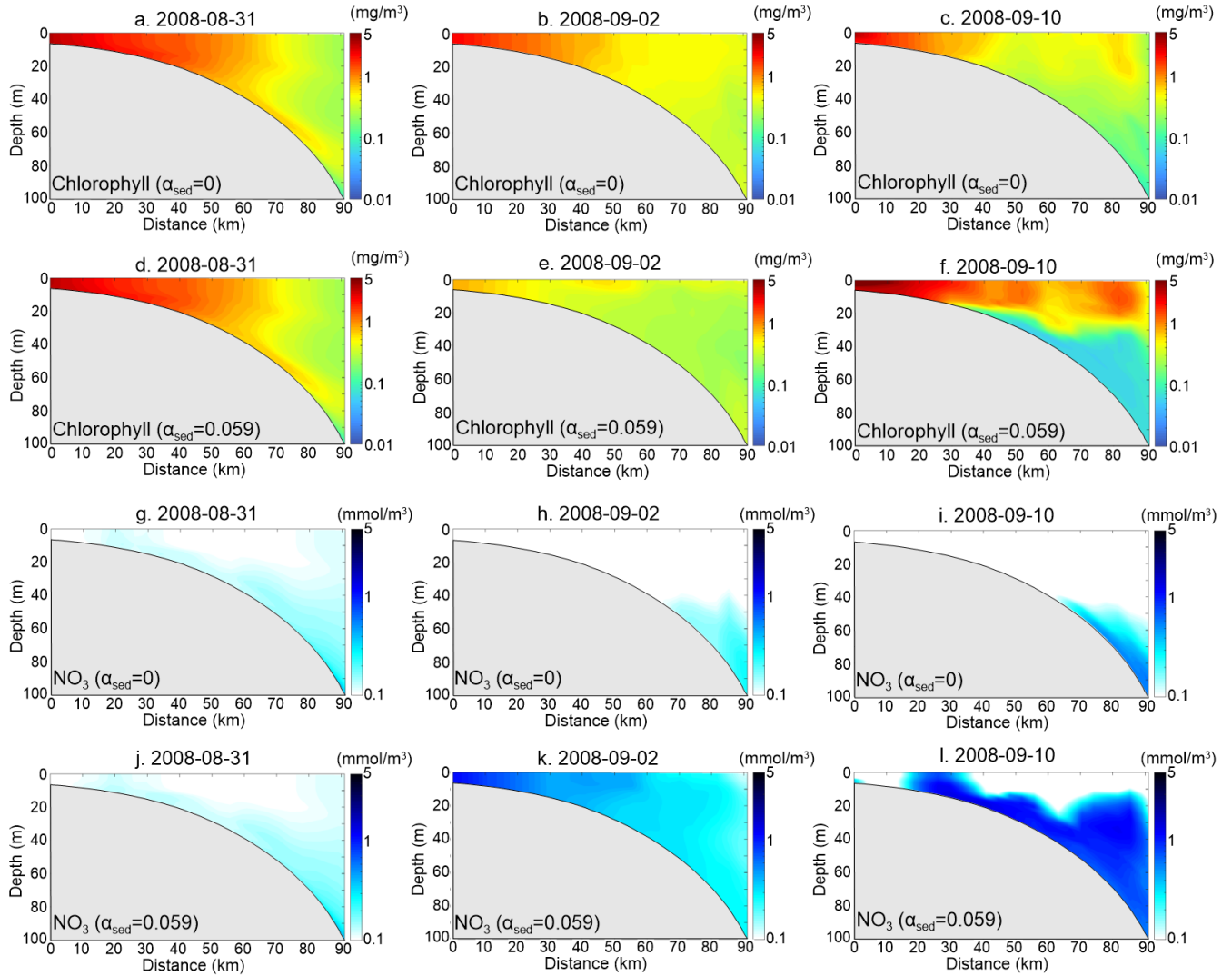
677
678

679 **Figure 5.** Time series of spatially averaged (inner shelf, water depth < 50 m) net primary
 680 production (a), surface chlorophyll concentration (b), surface NO₃ concentration (c), surface
 681 suspended sediment concentration (d), solar shortwave radiation (e), and sea surface temperature
 682 (f). In panels a, b, and c, blue represents benchmark run ($\alpha_{sed} = 0.059$) and red represents test 1
 683 ($\alpha_{sed} = 0$). Dots in panel (a) are daily-averaged net primary production. The black dashed line
 684 shows the time of Gustav landfall.
 685



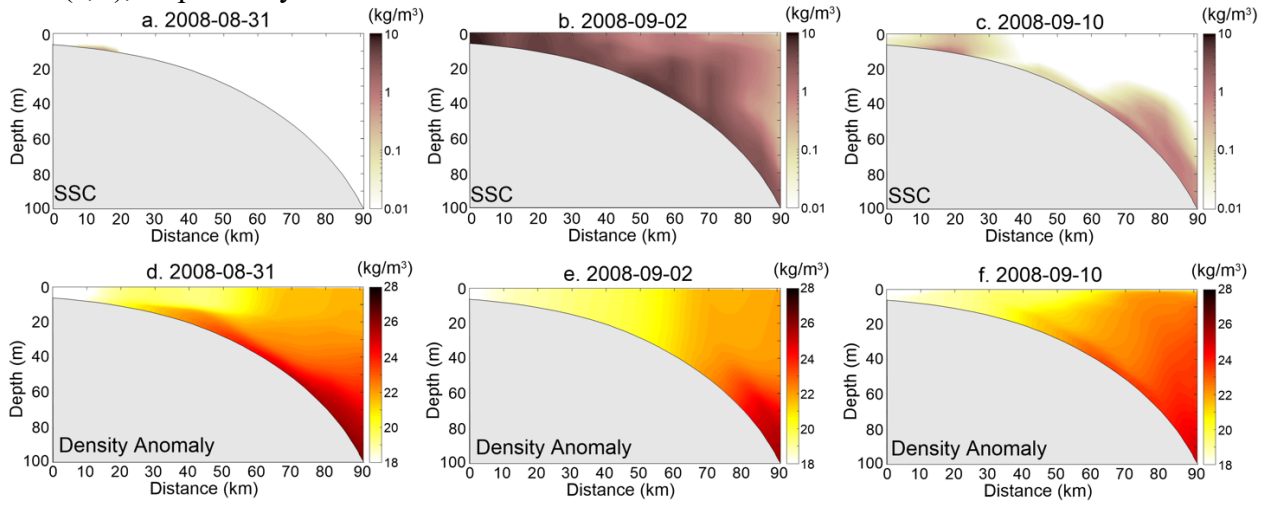
686
 687

688 **Figure 6.** Model simulated chlorophyll and NO₃ along transect D on August 31st (first column),
 689 September 2nd (second column), and September 10th (third column). The first and second rows
 690 represent chlorophyll concentration of the test 1 and benchmark run, respectively (note the color
 691 scale is different from Fig. 3). The third and fourth rows show NO₃ concentration of test 1 and
 692 benchmark run, respectively.
 693



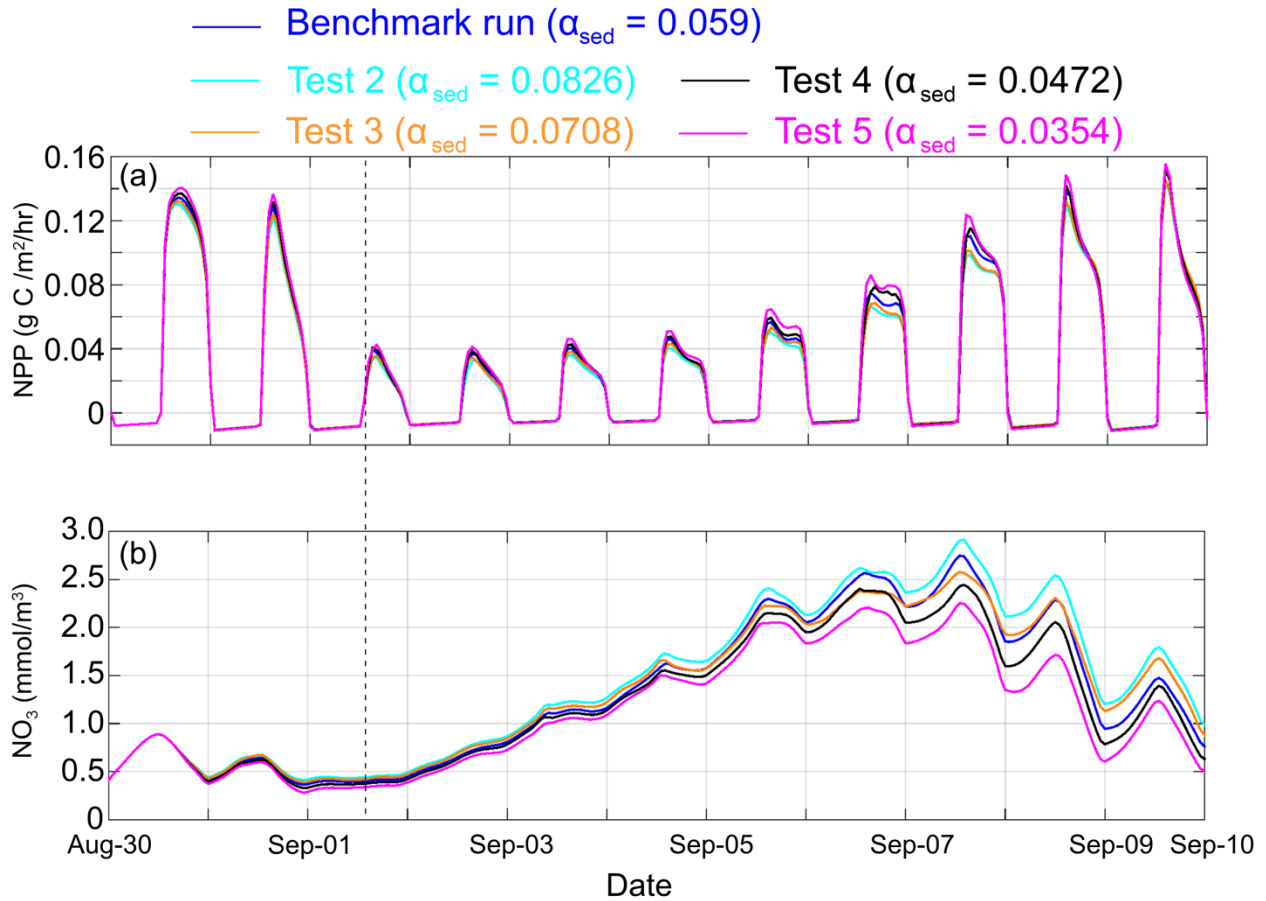
694
 695
 696

697 **Figure 7.** Model simulated suspended sediment concentration (SSC; first row) and water density
698 anomaly (second row) along transect D on August 31st (a, d), September 2nd (b, e), and September
699 10th (c, f), respectively.



700

701 **Figure 8.** Comparison of spatial averaged (inner shelf, water depth < 50 m) net primary production
 702 (panel a) and NO₃ concentration (panel b) between benchmark run (blue) and sensitivity tests with
 703 different α_{sed} (test 2: cyan; test 3: orange; test 4: black; test 5: magenta). The black dashed line
 704 shows the time of Gustav landfall.
 705



706
 707

708 **Table 1.** Offshore fluxes of NO₃ and chlorophyll along the 50-m isobath transect (see location
 709 in Fig. 1b).

710

Model Runs	Net offshore NO ₃ flux (mmol N/m/s)	Net offshore Chl flux (mg/m/s)
benchmark run ($\alpha_{sed} = 0.059$)	38.71	43.10
test 1 ($\alpha_{sed} = 0$)	7.35	66.88

711

712